DEVELOPMENT OF A MID-FIDELITY AEROELASTIC COUPLING FRAMEWORK FOR ANALYZING ROTOR-AIRFRAME INTERACTIONS

Moritz Linder* Muhammed Kürşat Yurt* Jonas John* Ilkay Yavrucuk**

*Graduate Research Assistant **Professor and Department Head

Institute for Helicopter Technology and VTOL

Technical University of Munich, 80333 Munich, Germany

In this paper coupled mid-fidelity simulations are performed to analyze aeroelastic interactional behaviour between rotor and empennage. To be able to simulate the interactional behavior, two coupling approaches are implemented and tested in this work. The first approach is a periodic loose coupling between the freewake solver UPM and a structural modal solver with a line based mapping. The second approach is a time-resolved coupling between UPM and a structural modal solver with a 3D surface mapping. The investigations show promising results compared to flight test data and thus provide a good commencement for further research.

NOTATION

Symbols

C_p	Pressure coefficient
$\mathbf{D}$	Damping-matrix
$\mathbf{D}_{mod}$	Modal damping-matrix
D_n	Damping constant of mode n
$\mathbf{F}$	Load vector
$\mathbf{F}_{mod}$	Modal load vector
$\mathbf{K}$	Stiffness-matrix
$\mathbf{K}_{mod}$	Modal stiffness-matrix
$\mathbf{M}$	Mass-matrix
$\mathbf{M}_{mod}$	Modal mass-matrix
N	Number of degrees of freedom
N_b	Number of blades
$\mathbf{x}$	Displacement vector
$\boldsymbol{\zeta}$	Damping vector
ζ_n	Modal damping coefficient of mode n
$\boldsymbol{\xi}$	Modal displacement vector
$\boldsymbol{\Phi}$	Eigenvector
ω	Natural eigenfrequency
$\boldsymbol{\omega}$	Frequency vector
ω_n	Eigenfrequency of mode n

Acronyms

AHD	Airbus Helicopters Germany
BPF	Blade passing frequency
CFD	Computational fluid dynamics
CSD	Computational structural dynamics
DLR	German Aerospace Center
DoF	Degree of freedom
CFD	Computational fluid dynamics
ELFU	Elastic fuselage
FE	Finite element
FM	Flight mechanics
FT	Flight test
p2p	Peak-to-peak
UPM	Unsteady Panel Method

1 INTRODUCTION

The aerodynamic interactions between a helicopter's main rotor and other components, like the fuselage and empennage, constitute some of the most intricate phenomena in helicopter research, thus making them a critical area of study in helicopter development [1]. While advancements in numerical methods offer the potential for more in-depth analysis and the development of suitable solutions, accurately predicting these interactions remains a significant challenge [2, 3]. As a result, interactions involving the main rotor, airframe, and empennage often necessitate design adjustments during flight testing due to potential flight instability or compromised comfort [4]. These changes during testing are both time-consuming and costly, highlighting the need to model and assess these interaction effects during the early design phases.

To address this, the current study proposes implementing a coupling environment that integrates a mid-fidelity aerodynamics solver with a structural modal solver, aiming to comprehensively and efficiently model these interaction effects in helicopter systems.

Among various interactional phenomena, three flight states hold paramount importance: hovering flight, slow-forward flight, and fast-forward flight. Slow-forward flight can trigger phenomena like pitch-up during the transition from hover to forward flight. This maneuver induces abrupt changes in main rotor thrust, resulting in substantial alterations in downwash and pitching moment, subsequently affecting the helicopter's attitude. However, the focus of this paper predominantly centers on the tail interferences, primarily observed during fast-forward flight with sometimes slight climb or descent rates.

The aerodynamic interactions acting on the empennage are particularly significant and require increased analysis. It has been shown many times in the past that the empennage design can cause problems in terms of stability and control due to the large forces and moments generated at the tail by unsteady loading. This large influence is due to the fact that the horizontal and vertical stabilizer (fin) contribute significantly to the static and dynamic stability of the helicopter. Regarding the influence of the main rotor wake on the empennage, several studies were conducted in the 1980s and 1990s which showed that there is a clear relationship between the unsteady loads and vibration levels at the empennage and the relative position of the tail surfaces to the main rotor wake. In particular, the effect of the horizontal stabilizer is influenced and altered by the rotor wake's relative position. The non-uniform three-dimensional flow distribution at the empennage can result in the excitation of significant vibrations [5].

Besides the main rotor wake, the wake of the fuselage, fairings and rotor mast is also of great importance when considering the aerodynamic interactions at the tail. These interference effects manifest themselves primarily as a reduction in the effectiveness of the horizontal and vertical stabilizer, as well as significant dynamic structural loads and vibrations that can also cause tail-shake [6, 7]. Tail-shake is characterized by strong lateral vibrations, which, depending on the severity, have a serious effect on the helicopter stability and comfort. In several helicopter designs the primary cause of tail-shake was the interaction between the tail structure and the wake of the rotor, fuselage and fairings (see Figure 1) [8, 9]. The phenomenon is characterized by various influencing factors, such as the aerodynamic design of the rotor hub, the pylon, the engine inlet, outlet and cowlings, as well as the shape, positioning and structural dynamics of the tail boom. Depending on these factors, the aerodynamic interactions can result in excitations of low-frequency eigenmodes of the helicopter structure in certain flight conditions [10]. Typically these vibrations are in a frequency range of 1 to 2/rev (the rotor frequency is typically in the range of 3-6 Hz), which corresponds to a frequency that is particularly uncomfortable for humans [8, 11]. Another characteristic of the tail-shake phenomenon is its highly unsteady nature. It is often described as random lateral 'kicks' [8].

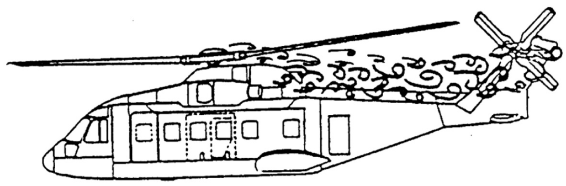

Fig. 1: Schematic illustration of the aerodynamic interactions causing tail-shake [8]

Despite extensive manufacturer expertise in helicopter design, tail-shake frequently occurs for new helicopter designs. One of the main problems is, that it is usually not recognized until the first flight tests. For a large number of helicopters interaction problems are documented during prototype stage such as for the EH-101 [12], the Tiger [13], the SA365N [14], the CH-53E, UH-60A and S-76 [15], the BK-117 [16] and the EC-135 [17]. This shows the large gap in knowledge regarding the causes and parameters of this phenomenon, as well as the lack of a reliable early prediction and analysis methods. In all examples mentioned, elaborate wind tunnel tests were carried out, which are costly and can sometimes have reliability problems due to the necessary simplifications of the models. This further emphasizes the great need for numerical simulation methods for the analysis of such interaction phenomena [10].

Notably, employing high-fidelity viscous simulation techniques such as Computational Fluid Dynamics (CFD) in conjunction with holistic helicopter models has proven effective in representing flow phenomena and interactions, both in the low-frequency range relevant for tail-shake and in the high-frequency range caused by blade passage interactions [18–20]. Alternatively, transient panel methods have demonstrated favorable results in approximating high-frequency phenomena within a fraction of the computational time [21].

Beyond accurate flow field representation, accurately modeling the helicopter's structure and its elasticity remains pivotal for precise interaction calculations. This is due to the fact that aerodynamic loads induce structural deformation and potential vibrational excitations, reciprocally influencing aerodynamic loads. In [22], a coupling between high-fidelity CFD and a structural solver has been implemented to accurately replicate interaction phenomena. This enabled resolution of resonances, aerodynamic damping, and alterations in aerodynamic loads, facilitating thorough analysis of the tail-shake phenomenon in the Bluecopter™ Demonstrator. However, this approach entails extensive computation and model setup times, limiting its practicality in optimization processes during the design phase.

Consequently, two coupling approaches using an aerodynamics solver founded on a panel method are implemented in this work. The first approach is a periodic loose coupling between the freewake solver UPM and a structural modal solver with a line based mapping based on the work of *Rex et. al* [21, 23]. The second approach is a time-resolved coupling between UPM and a structural modal solver with a 3D surface mapping. The coupling framework is planned to enable an analysis of large parts of the flight envelope already in early development phases and to identify potentially problematic flight conditions that can then be analyzed in more detail with higher-fidelity methods.

2 SIMULATION FRAMEWORK

2.1 FLIGHT TEST REFERENCE DATA

The reference helicopter used for the investigations in this paper is the light medium, twin-engine research helicopter Bluecopter™ from Airbus Helicopters (see Figure 2). The Bluecopter™ was developed as a demonstrator to test future eco-friendly concepts and green technologies, and to provide a basis for the validation of numerical methods through the test data [24].

Fig. 2: Reference helicopter Bluecopter™ Demonstrator from Airbus Helicopters

The Bluecopter™ is ideally suited for validation and assessment of numerical methods, as an extensive flight test campaign was conducted by Airbus Helicopters. In the campaign the helicopter was equipped with additional instrumentation, including various sensors for measuring vibrations, unsteady pressures, and bending moments at the empennage to gain insight into the behavior of tail interference phenomena. The sensors used and their locations can be seen in Figure 3. For the T-tail vibrations one sensor each for the z-vibrations is placed on the left and right side (VTTFLZ/VTTFRZ). Furthermore two strain gauge sensors for the measurement of the flapwise bending moment of the T-tail are used ($M_{\beta,L}/M_{\beta,R}$). Additionally a three-way sensor (VFINF) was mounted at the top front of the fin for measuring the respective vibrations.

The unsteady pressure sensors were placed at twelve positions distributed over the T-tail and fin (see Figure 3b) in order to be able to determine the loading of the empennage. Three pressure sensors were placed on each side of the fin at the thickest part of the airfoil (FL1-FL3 and FR1-FR3). Care was taken to place the sensors directly opposite to each other so that the pressure difference between the pressure and suction side could be easily calculated. On the T-tail, such a pair of sensors was positioned at 72% of the span and 22% of the chord length on each side (U1/L1 and U2/L4). On the lower side of the T-tail, an additional sensor was placed on each side at 39% of the span. The pressure sensors used are differential pressure sensors that

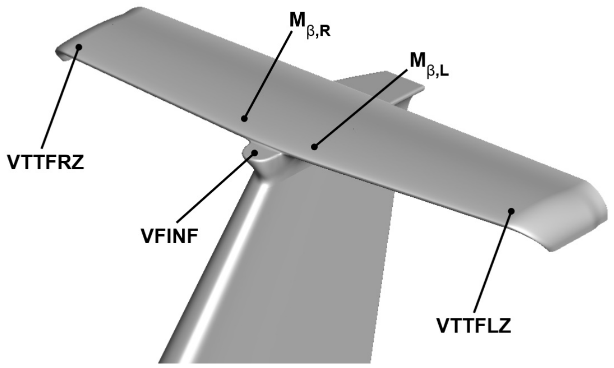

(a) Vibration and strain gauge sensors

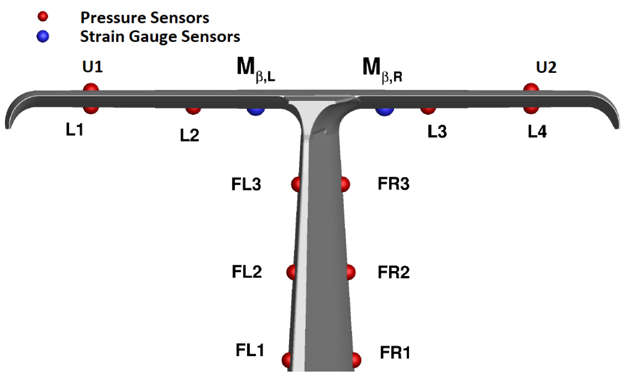

(b) Unsteady pressure and strain gauge sensors (from behind) [21]

Fig. 3: Locations of the empennage vibration, unsteady pressure, and strain gauge sensors

measure the pressure difference with respect to the interior volume of the stabilizers. Small holes were drilled so that the pressure in the interior volume can adapt to the ambient pressure, depending on the altitude [21]. One pressure sensor each inside the T-tail and the fin measure the reference pressure, which is used for the differential calculation. By using the differential pressure sensors, a wide bandwidth of pressure variations can be analyzed. Since the empennage was manufactured prior to instrumentation, the sensors and wiring had to be attached to the exterior (see Figure 4). The pressure sensors were covered with small plates in the process. In [21] it is shown that these fairings have a non-negligible influence on the mean pressure values.

During flight tests, no major interaction problems were encountered. However, increased vibrations with slight tail-shake were encountered in one flight state. This flight state (TOP36) is a fast forward flight with a slight descent. As a result, the TOP36 flight state is characterized by a low thrust requirement and consequently a low anti-torque compensation. The descent rate and the low induced velocities by the main rotor cause the rotor wake to impinge on the empennage, resulting in strong interference. The helicopter is oriented in a slight nose down position and a side-slip angle of nearly zero.

Fig. 4: Pressure sensor instrumentation at the Bluecopter^{TM} empennage [21]

2.2 FREEWAKE SOLVER

For the investigations carried out here the Unsteady Panel Method (*UPM*) is used. UPM is an unsteady three-dimensional panel free wake code developed by the German Aerospace Center (DLR) Institute of Aerodynamics and Flow Technology [25, 26]. The code uses a velocity-based indirect potential formulation. In modeling the individual components, a distinction is made between lifting components and non-lifting components. Lifting components (i.e. rotor blades, wings, and stabilizers) are modeled by a combination of a source/sink distribution with quadrilateral panels on the component surface and a vortex-lattice on the camber surface (see Figure 5). The source/sink distribution accounts for the thickness effect and the vortex-lattice describes the lift of the component. For the generation of the wake, short zero-thickness extensions (2% of the local chord-length) of the trailing edge (Kutta panels) are used (tangential to the camber surface), which shed a full-span free wake of connected vortex filaments. The evolution of the wake is computed by explicit time stepping. Non-lifting bodies are modeled by quadrilateral and/or triangular surface panels with a constant source/sink strength. Thus, only the displacement effect on the flow is modeled, but not lift and drag [25, 27].

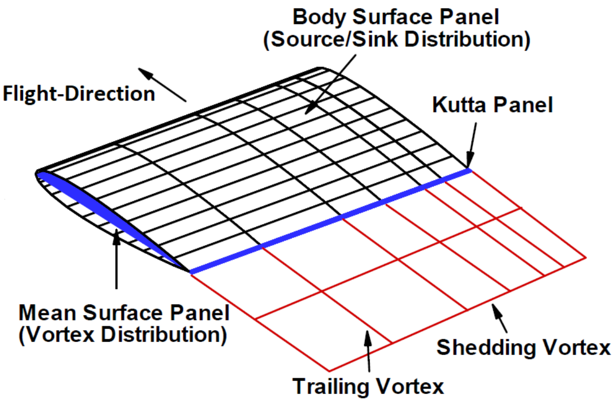

Fig. 5: Schematic illustration of the modeling of lifting components in UPM [21]

For the lifting surfaces, a new wake strip is generated at each time step and added to the existing wake panels. The wake consists of a series of quadrilateral vortex rings released from the trailing edge of the Kutta panels. The strength of these emitted wake panels is the same as the strength of the Kutta panels and remains constant over the time course of the simulation. After the wake is formed, it is transported and deformed according to the local flow conditions. To calculate the velocities induced by the wake, an implemented tip vortex rollup model can optionally be used [28, 29].

For the computation of the positioning of the wake panels, a predictor-corrector method based on so-called multistep-methods is used in UPM. For the predictor step the explicit Adams-Bashforth method is used and for the corrector steps the implicit Adams-Moulton method [28].

2.3 FREEWAKE MODEL

The UPM model of the Bluecopter^{TM} is shown in Figure 6. It can be seen that in the model some simplifications are made. For example, neither the rotor hub is modeled, nor is the connecting piece between the horizontal and vertical stabilizer, as these would make the model much more complex in terms of defining component motions. Additionally, openings such as the engine inlets and outlets and the Fenestron duct are closed. Since flow separations cannot currently be modeled in UPM, modeling out these openings would only increase the complexity of the model without being able to represent the relevant flow phenomena that occur there.

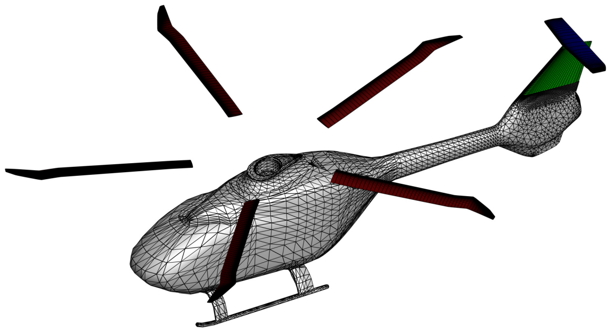

Fig. 6: UPM model of the Bluecopter^{TM} with main rotor (red), airframe (grey), horizontal stabilizer (blue) and vertical stabilizer (green)

As shown in Figure 6, an unstructured mesh with source/sink panels is used for the airframe to model the displacement effects. For the lifting surfaces (i.e. rotor blades, T-tail, and fin), the modeling approach described in section 2.2 is used. Therefor, the components are divided into segments in spanwise direction, which are then discretized again in chordwise direction. The concrete discretization of the individual model components is listed in Table 1.

Table 1: Discretisation of the Bluecopter^{TM} UPM model

Comp.	N_b	Panels Spanwise	Panels Chordwise	Panels Total
Main rotor	5	50	30	7500
T-Tail	2	30	25	1500
Fin	1	30	30	900
Airframe	–	–	–	11351
				21251

For the wake modeling, UPM's full-span wake is used so that vortex-rollup is obtained by itself without calibrating a rollup model. *Johnson* [6] recommends that when modeling the vortex sheets, the vortex core radii should be defined so that they touch or slightly overlap at adjacent panels. However, for flight conditions with strong interactions, it may be advantageous to choose larger core radii and increase core smoothing to increase numerical stability. But if smoothing is applied excessively, the results can be degraded and pressure peaks are not properly captured. Therefore, the core radii of the full-span wake elements were chosen to overlap slightly in the outer region. Since the spanwise discretization becomes coarser for the panels further inside, the core radius was set to larger values here. To enhance the core smoothing, the Kaufmann-Scully model was chosen as the vortex core model. The models for the vortex-rollup, the stall correction and the consideration of compressibility effects according to Prandtl-Glauert are deactivated. In Figure 7 an exemplary UPM simulation of the used UPM model is visualized, with the generated rotor and empennage wake.

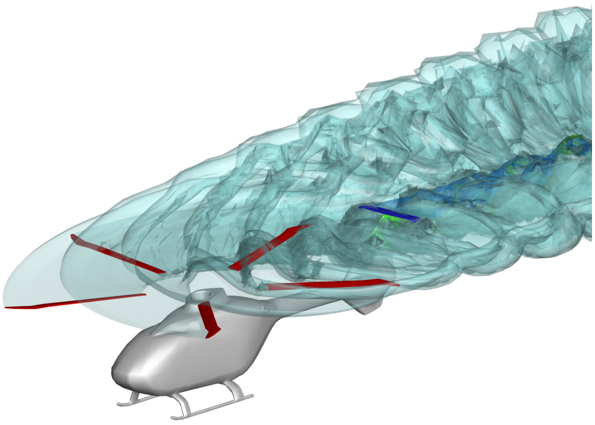

Fig. 7: UPM simulation with rotor and empennage wake

2.4 STRUCTURAL SOLVERS

In order to be able to model the overall behavior of a helicopter and, above all, the interactional behavior, it is of great importance to also simulate the structural dynamics of the helicopter with a computational structural dynamics (CSD) solver. Of particular interest in this context are the structural eigenmodes and frequencies. A widely used method for identifying the eigenmodes and frequencies is the modal analysis.

The dynamic behavior of a system with multiple DoFs N can be expressed by the following equation of motion [30]:

$$\mathbf{M}\ddot{\mathbf{x}}(t) + \mathbf{D}\dot{\mathbf{x}}(t) + \mathbf{K}\mathbf{x}(t) = \mathbf{F}(t) \tag{1}$$

with:
M = Mass-matrix $(N \times N)$
D = Damping-matrix $(N \times N)$
K = Stiffness-matrix $(N \times N)$
x = Displacement vector
F = Load vector

Assuming small displacements, the structural behavior can be assumed to be linear, which allows linearization of the matrices. Since the physical damping characteristics are often unknown, a definition of the damping matrix **D** is circumvented by defining the damping later in modal space. Using a harmonic approach for the displacement vector and neglecting the damping, the following equation is obtained for the free-vibration [30]:

$$(\mathbf{K} - \omega^2 \mathbf{M})\,\mathbf{\Phi} = 0 \tag{2}$$

with:
ω = Natural eigenfrequency
$\mathbf{\Phi}$ = Eigenvector

For the definition of the damping constant D_n in modal space, equation 3 is used. The modal damping ζ_n is determined empirically and is usually between 1 and 10% [10].

$$D_n = 2\omega_n \zeta_n \tag{3}$$

From the individual modal values, the corresponding matrices from equation 1 can be formed in modal space, and together with the modal displacements $\boldsymbol{\xi}$, equation 1 can be transformed into modal space:

$$\mathbf{M}_{mod}\ddot{\boldsymbol{\xi}}(t) + \mathbf{D}_{mod}\dot{\boldsymbol{\xi}}(t) + \mathbf{K}_{mod}\boldsymbol{\xi}(t) = \mathbf{F}_{mod}(t) \tag{4}$$

$$\ddot{\boldsymbol{\xi}}(t) + 2\boldsymbol{\omega}\boldsymbol{\zeta}\dot{\boldsymbol{\xi}}(t) + \boldsymbol{\omega}^2\boldsymbol{\xi}(t) = \mathbf{F}_{mod}(t) \tag{5}$$

with:
$\mathbf{M}_{mod}$ = Modal mass-matrix $(N \times N)$
$\mathbf{D}_{mod}$ = Modal damping-matrix $(N \times N)$
$\mathbf{K}_{mod}$ = Modal stiffness-matrix $(N \times N)$
$\mathbf{F}_{mod}$ = Modal excitation
$\boldsymbol{\xi}$ = Modal displacement vector
$\boldsymbol{\omega}$ = Frequency vector
$\boldsymbol{\zeta}$ = Damping vector

The advantage of formulating the problem in modal space is the possibility to reduce the calculation effort through modal reduction.

In the current work two different structural modal solvers are used for the different coupling approaches. The first modal solver is the *elastic fuselage* (ELFU) developed by *Rex* in-house at the Institute for Helicopter Technology and VTOL at the Technical University of Munich [31, 32], which was implemented in a flight mechanics (FM) solver. The reason for the usage of the second solver is that the elastic fuselage was primarily developed for efficient and fast modeling of structural effects on low frequency flight mechanics and interactions with auto-pilot modes. Its interfaces are not prepared for time-resolved aerodynamic forces exchange. Therefore the second structural solver *HTModal* was used for the second coupling approach. HTModal is the current in-house structural modal solver at the Institute of Helicopter Technology and VTOL at the Technical University of Munich and was developed specifically for the application in a time-resolved coupling framework.

2.4.1 Structural Solver ELFU

The elastic fuselage (ELFU) is a modal solver developed at the Institute for Helicopter Technology and VTOL at the Technical University of Munich. It is integrated into a FM solver, and makes it possible to model the entire elastic airframe. To create the modal model, a modal analysis of a finite element (FE) model of the helicopter is performed to determine the mode shapes and eigenfrequencies of the helicopter structure. Commercial structural solvers such as *NASTRAN* are typically used for this modal analysis. The relevant eigenmodes and FE nodes are then selected for the modal model. For each mode, the eigenfrequency, the modal mass and its modal damping are specified. In addition, the corresponding eigenvector must be specified for each selected node in the respective mode. [31]

The integration of the ELFU into the FM time simulation is shown schematically in Figure 8. The coupling between FM and ELFU is a strong coupling in each time step. When the ELFU is activated, the calculated loads are passed not only to the rigid body motion but also to the ELFU. Furthermore it is possible to periodically apply external loads to the ELFU. For a more detailed description of the ELFU see [23,31,32].

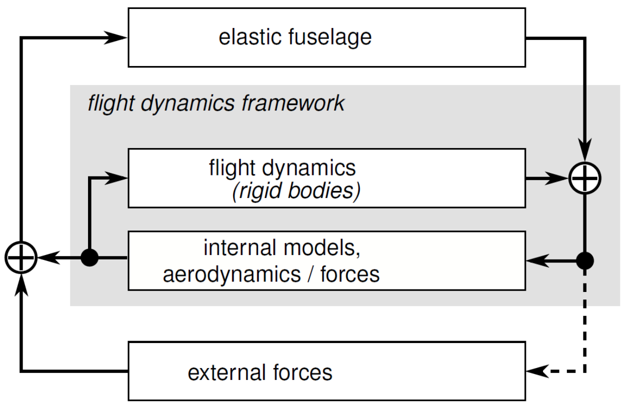

Fig. 8: FM-ELFU coupling framework [23]

2.4.2 Structural Solver HTModal

For the application in the time-resolved coupling framework the modal solver HTModal was developed at the Institute for Helicopter Technology and VTOL to be able to implement all the needed functionalities. The solver can be used to solve linear static and dynamic analysis problems. The dynamic calculations in HTModal are based on the equation of motion in modal space (see equation 5) and are performed with a second-order time integration. For the time integration several methods are implemented such as the Newmark-β method or the generalized-α method. To reduce the computational effort modal reduction can be performed by limiting the degrees of freedom to the relevant low-frequency range. Structural damping is applied according to equation 3 depending on the respective eigenfrequency ω_n. For specifying the modal damping coefficients ζ different approaches are included. The damping coefficient can be either held constant for all eigenmodes or a damping matrix can be given setting a specific damping coefficient for each mode.

The HTModal input files are primarily based on *NASTRAN*'s linear eigenvalue analysis (SOL103) output files. It requires the mass matrix, the eigenvalues, and the eigenvectors along with the mesh data. If available the structural and viscous damping matrices can be used as an input as well for specifying the modal damping coefficients. These matrices are transformed from physical to modal space and then used for the calculations. The force vector is given by the coupling environment and converted to modal space as well. After the computation, the results are transformed back into physical space and stored in the output files of the modal solver.

2.5 STRUCTURAL MODELS

Since in this work the interaction phenomena occurring on the helicopter are investigated, with a focus on the influence of the structural behavior of the tail unit, the structural model is limited to the airframe. The basis for the modal model is a *NASTRAN* FE model (see Figure 9), with a number of 145,887 nodes and a concentration of the nodes in the tail boom and empennage region.

The FE model was primarily built for the simulation of simple structural mechanics problems and therefore contains some simplifications and neglects of parts. The influence of these parts on the investigation results was estimated to be small. For

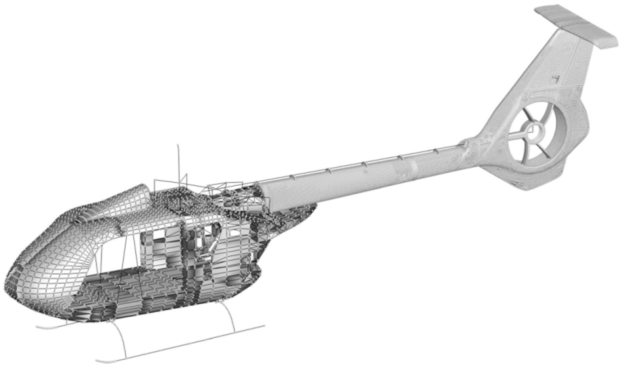

Fig. 9: *NASTRAN* FE model of the helicopter's airframe [22]

example, the model does not include rotating parts, doors and rotor covers. In addition, the load paths between main rotor and fuselage and between tail rotor and tail boom are modeled in a simplified way.

To obtain the mode shapes for the modal model, a linear eigenvalue analysis of the FE model is performed. The first six modes (rigid body modes) are not considered in this work. A modal convergence study by *Rex et al* [32] has shown that the first 40 modes represent the most dominant dynamics of the structure, corresponding to a natural frequency of up to 8/rev. Moreover, due to uncertainties regarding the structural dynamics, the reliability of the model decreases for higher frequencies, which is why frequencies above this 8/rev limit are not evaluated in this work. Regarding the structural damping, no concrete information is available. However, an estimate can be made based on shake tests of comparable airframe structures [22], which is why the damping of the individual modes is set to $\zeta = 4\%$. The relevant modes include the low-frequency bending modes of the tail boom (see Figure 10) in the frequency range around 1/rev, as well as the torsional modes of the tail boom with a frequency around 2/rev. The relevant modes of the T-tail are shown in Figure 11 and are in the range around 4/rev.

2.5.1 Structural Model ELFU

For the ELFU model a highly simplified and reduced structural model is used. The mesh is limited to 123 nodes, consisting of some obligatory nodes for the solver like the main rotor and tail rotor, the c/4 points of the horizontal and vertical stabilizer and several points along the top of the tail boom. This reduction of the model was done to reduce the computational effort and to simplify the linking between the UPM and the CSD model. To simplify the application of the aerodynamic loads in the CSD model, so-called RBE3 interpolation elements were added to the FE model,

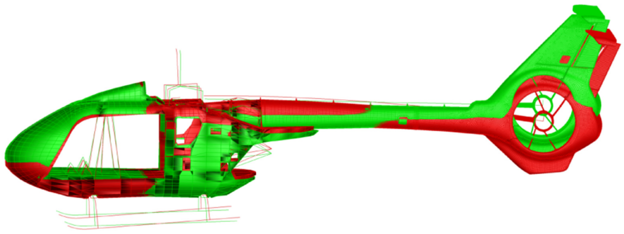

(a) First vertical bending mode

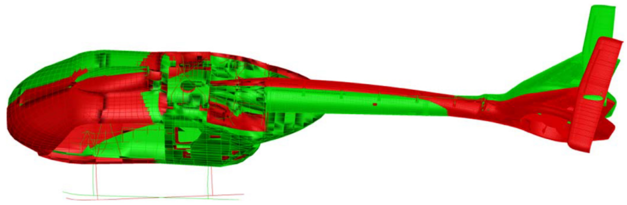

(b) First lateral bending mode

Fig. 10: Tail-shake relevant structural mode shapes [22]

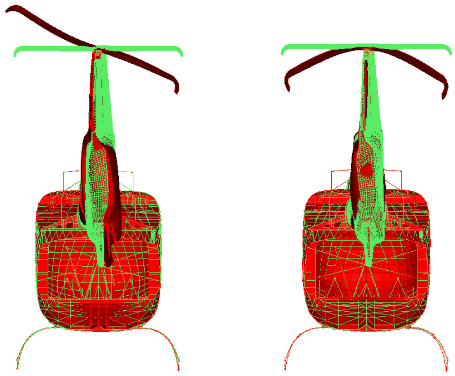

(a) Asymmetric T-Tail flap mode (b) Symmetric T-Tail flap mode

Fig. 11: Relevant mode shapes of the T-Tail [32]

representing the c/4 points. Since the focus lies on the loads of the lifting surfaces, these RBE3 elements are limited to the fin and the T-tail. The principle of using the RBE3 elements is shown schematically in Figure 12. The UPM results (forces and moments) are given for each segment in the c/4 point and are also applied in the structural model in these points. In order to establish a direct connection between these points and the actual structure of each segment, the RBE3 elements, whose center is located in the c/4 point, are used. Thus, a linking between UPM and CSD model can be established very easily and the line loads from UPM can be applied in the CSD model in a very simple way. In addition, the positions and deformations of these nodes of the CSD model can be used directly for the deformation definition in UPM. The additional sensor points on the tail boom are only used to model the deformation of the tail boom.

The CSD model itself is built from the selected

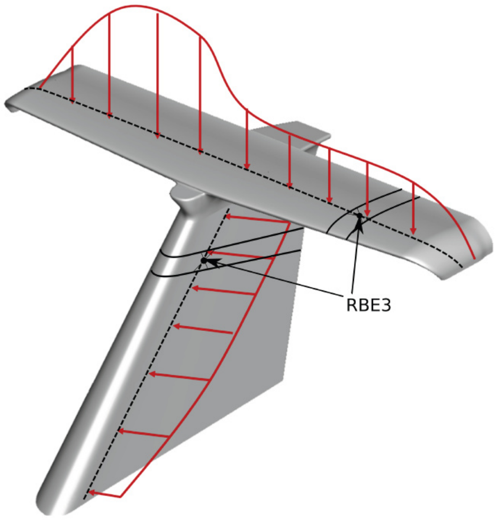

Fig. 12: Load interface at T-Tail: Application of aerodynamic loads in the CSD model via RBE3 elements [32]

mode shapes and the selected nodes (degrees of freedom). For each mode, frequency and damping (here always 4%) are defined, as well as the eigenvector (six DoF) for each selected node.

2.5.2 Structural Model HTModal

Since HTModal is used for the time-resolved 3D coupling, the HTModal model consists of all the nodes from the FE model (see Figure 13) and the corresponding modes. Like in the ELFU model, a constant modal damping coefficient of 4% is applied for every frequency.

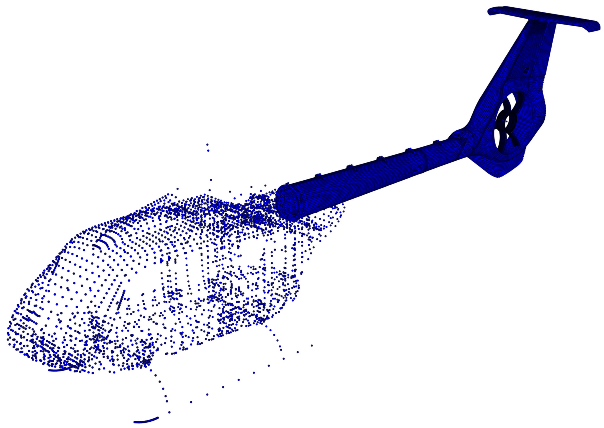

Fig. 13: Structural Model for HTModal

2.6 LOOSE UPM-CSD COUPLING FRAMEWORK

The first coupling approach developed in this work is a loose UPM-CSD coupling framework based on an existing FM-UPM coupling and the work of *Rex, Rinker* and *Ries* [21, 23]. Figure 14 shows the framework of the implemented loose UPM-CSD coupling. Prior to the structural coupling, a trim coupling (FM-UPM coupling) is performed to obtain an initial trim condition as a starting point for the structural coupling. *Loose* coupling in the case of this approach means that the results and data (i.e. loads and deformations) are exchanged periodically after the completion of the respective UPM and CSD simulation. Since only steady flight conditions are studied, this approach is applicable and still leads to a converged final state. Although the load curves oscillate and structural vibrations occur, convergence is still achieved due to the periodic character of the curves.

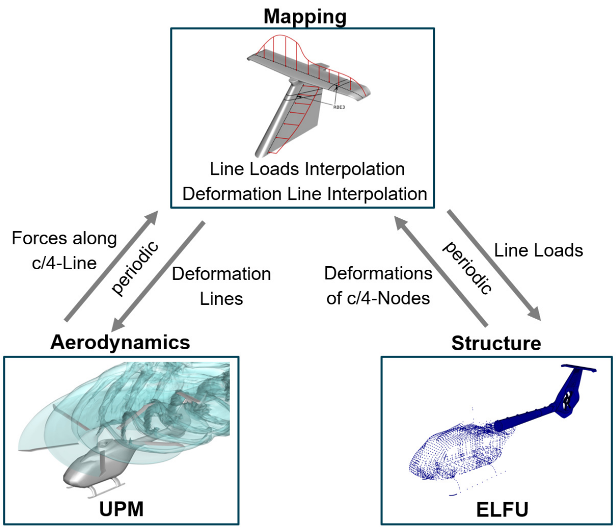

Fig. 14: Loose UPM-CSD coupling framework

As a first step of the coupling iteration, a CSD simulation is performed, initialized by the preceding trim results. To prescribe the UPM loads on the structural model the load curves at the individual components are required. To obtain these curves, the time histories over the last full rotor revolution of each segment are used. Since the load curves are not perfectly periodic, excitations of n/rev frequencies occur. To minimize this deviation and excitation, an interpolation treatment is used to ensure that the signal is as periodic as possible without distorting the results. For each segment, the load curves are evaluated in the c/4 point. Thus, for each time step of the rotor revolution, line loads of the respective load component are obtained over the span. These load curves in the c/4 points can then be directly applied to the corresponding nodes of the structural model. To obtain this simplified application, the RBE3 elements were introduced during the generation of the structural model. The results of the CSD simulation are the displacements and rotations of the structural nodes.

These deformation curves are used to model elastic deformations in UPM. For this purpose, so-called bending lines are defined. The bending lines are a series of nodes with coordinates in the undeformed state. The displacements and rotations are then prescribed at these nodes and projected onto the surface mesh of the components. In the loose coupling implemented here, these bending lines are formed from the nodes of the structural ELFU model. Since the tail boom nodes are only defined up to the beginning of the Fenestron, the bending line and the deformations have to be extrapolated aft. With this deformation definition and the predefined trimmed flight state results, the UPM simulation is performed. As a result, the time history of the aerodynamic loads is obtained, which is used for setting up the CSD simulation in the next iteration step.

2.7 TIGHT UPM-CSD COUPLING FRAMEWORK

The second coupling approach developed in this work is a tight UPM-CSD coupling framework based on *preCICE* which is an open-source coupling library for partitioned multi-physics simulations [33]. Figure 15 shows the framework of the implemented tight UPM-CSD coupling. For the trim data, such as the attitude angles and the blade motions, the results from the loose coupling trim are used to have comparable results. *Tight* coupling in the case of this approach means that there is a time-resolved data exchange between UPM and HTModal. In addition to that a 3D mapping is used to exchange the surface loads along with the displacements and velocities of the surface nodes.

To facilitate the process, the tight coupling framework utilizes the coupling library preCICE. It provides several coupling schemes and mapping algorithms. For the used coupling between UPM and HTModal a serial implicit coupling scheme with nearest neighbour mapping is used. In Figure 16 the mapping of the displacements from the HTModal mesh to the UPM mesh is exemplarily shown for the empennage.

To ensure a correct mapping a model conversion routine was additionally implemented to improve and facilitate the mapping between different meshes and avoid mapping errors due to different coordinate or unit systems. In figure 17 the match between the UPM and HTModal mesh is shown after the model conversion.

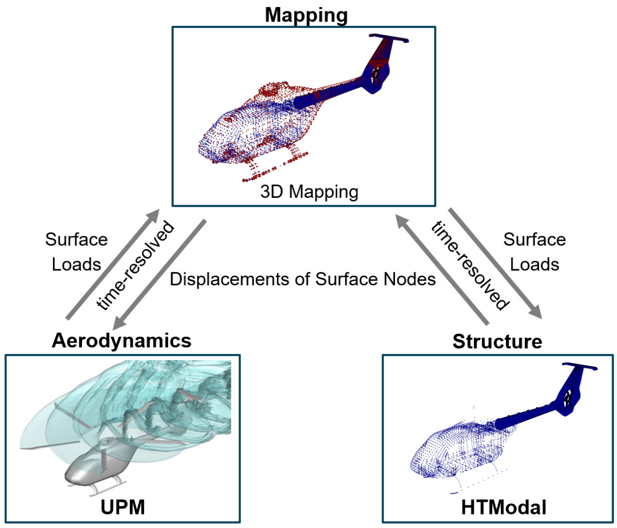

Fig. 15: Tight UPM-CSD coupling framework

For the UPM side of the coupling two different coupling meshes are used. The first mesh consists of the collocation points of the panels and is used for exchanging the aerodynamic forces. The second mesh consists of the panel corner points and is used to apply the displacements and velocities fed back from HTModal. The main rotor is not included in either of the meshes since the focus of this work lies on investigating the interactional behaviour of the tail section. Therefore the corner point mesh only consists of the fuselage, the tail boom, and the horizontal and vertical stabilizer. The collocation point mesh is further reduced and includes only the horizontal and vertical stabilizer. This reduction is chosen because at the moment due to the modeling simplifications in the panel approach and potential theory, the surface loads on non-lifting bodies are expected to deviate strongly from test data. Therefore, only the loads on the lifting surfaces are taken into account.

During the coupling process the forces are fed from UPM to HTModal in each coupling time step and the displacements and velocities are fed back from HTModal to UPM. For the coupling time step a main rotor azimuth of 8° is chosen which corresponds directly with the chosen UPM time step. This step size enables to resolve all relevant frequencies and at the same time speeds up the simulation time. To ensure an error free computation on the structural side, a smaller time stepping is chosen.

3 RESULTS

The flight condition investigated in this paper is the TOP36 descent flight. Figure 18 shows the result of

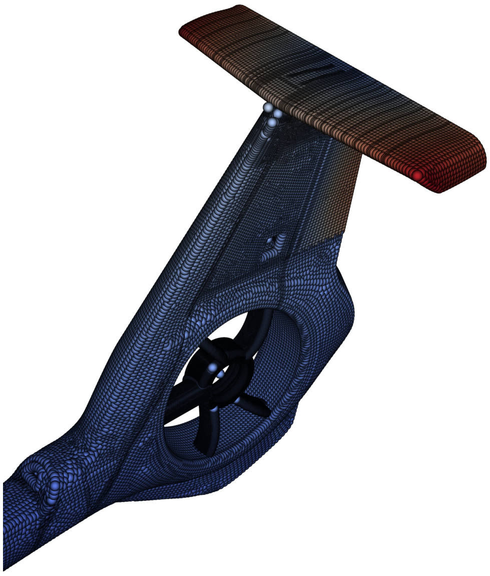

(a) Displacements on HTModal mesh

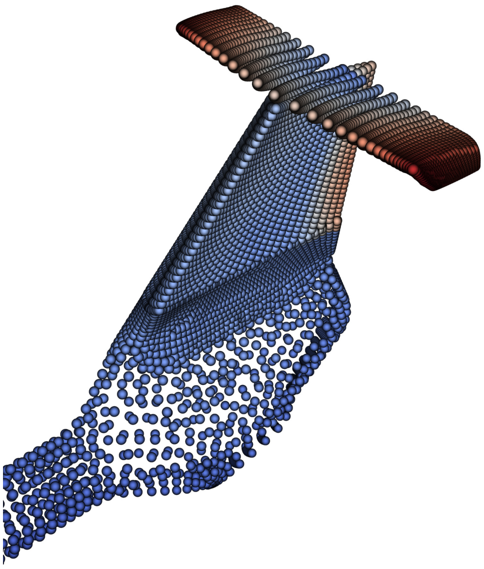

(b) Displacements on UPM mesh

Fig. 16: Mapping of the empennage displacements from HTModal mesh to UPM mesh

the associated UPM simulation to visualize the flight condition. It can be clearly seen that due to the descent rate superimposed on the forward speed, the rotor wake directly impinges on the fin and the T-tail which leads to strong aerodynamic interactions at the empennage.

In Table 2 the attitude angles of the helicopter during the flight test are compared to the calculated attitude angles of the coupling framework. For the attitude angles from the flight test data, the mean values are used. When comparing the coupling results with the flight test data, significant deviations can be seen in the pitch and roll angles (not in the

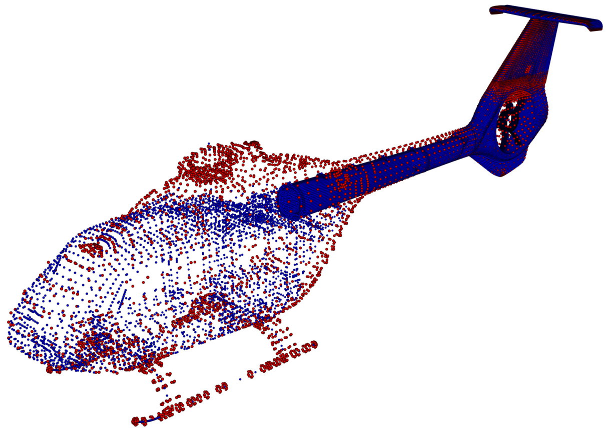

Fig. 17: Comparison of UPM mesh (red) and HTModal mesh (blue)

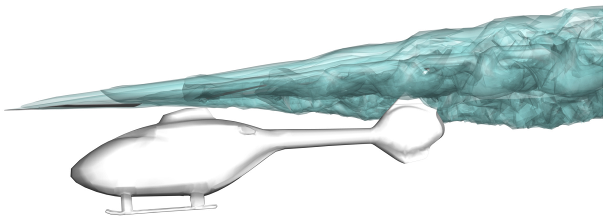

Fig. 18: Visualization of the UPM simulation of flight state TOP36

yaw angle, since this is specified as a simulation input). This discrepancy is partly due to the implementation of the trim coupling and partly due to the fact that UPM cannot map flow separations like the fuselage wake which has a clear influence on the flow at the empennage (see [22]) and thus leads to deviating fuselage loads and aerodynamic interferences. These attitude angle differences result in discrepancies with respect to the calculated pressures, loads, and deformations. However, these aspects will be discussed in more detail in the following sections.

Table 2: Comparison of helicopter attitude angles between flight test and coupling for TOP36

	Flight test	Coupling
Side slip angle [deg]	0.64	0.64
Pitch angle [deg]	-3.3	-1.1
Roll angle [deg]	2.13	-0.89

3.1 AERODYNAMIC LOADS

In the first step of the assessment, the calculated empennage loads of the two coupling approaches are analyzed and compared with the loads from the trim coupling. For this purpose, the curves of the total loads of the individual empennage components are considered (see Figure 19), as well as the peak-to-peak (p2p) values (see Table 3). For the two T-tail sides, the force in z-direction is considered, and for the fin, the force in y-direction. The force values are normalized by the loose coupling p2p values of the fin force. In Figure 19 it can be seen that the force curves are qualitatively and quantitatively very similar when comparing trim and loose coupling. Besides, a slight negative offset of the loose coupling values compared to the trim coupling values can be seen. This could possibly be explained by the small static deformation of the tail boom and the resulting change in relative position of the empennage with respect to the rotor wake. In addition, the clear asymmetry of the T-tail loads between the right and left sides described by *Rinker et al* [21] is evident from the graphs. The reason for this asymmetry is primarily the interference of the wake with the empennage [21].

In addition to the load level, the amplitudes of the load curves between the right and left T-tail side are also significantly different, with higher amplitudes on the left side. This difference in p2p values is also due to the interference of the fin and T-tail with the wake. On the left T-tail side, the wake impinges on the T-tail directly, whereas the right side is shielded by the fin. This effect is exacerbated by the asymmetric wake geometry caused by the higher downwash on the advancing blade side. When comparing the p2p values between trim and loose coupling, no major differences can be seen.

Comparing the results of the tight coupling with the results of the other two simulations, more obvious differences can be seen. The load level is in the same order of magnitude, but a more pronounced offset than between loose coupling and trim simulation can be seen here, which is probably due to the differences in the deformations. In addition, a clear phase shift compared to the trim and loose coupling can be seen. The cause of this shift could possibly be attributed to the difference in deformation behavior, but the reason for this phenomenon could not be clearly determined and requires further investigation. With respect to the amplitude and the p2p values, a reduction can be seen for the tight coupling (see also table 3), which suggests an increased aerodynamic damping for this method. It must be noted at this point that the modal damping of 4% for ELFU also includes a part of the modelling of the aerodynamic damping. Thus, the damping value of 4% for HTModal

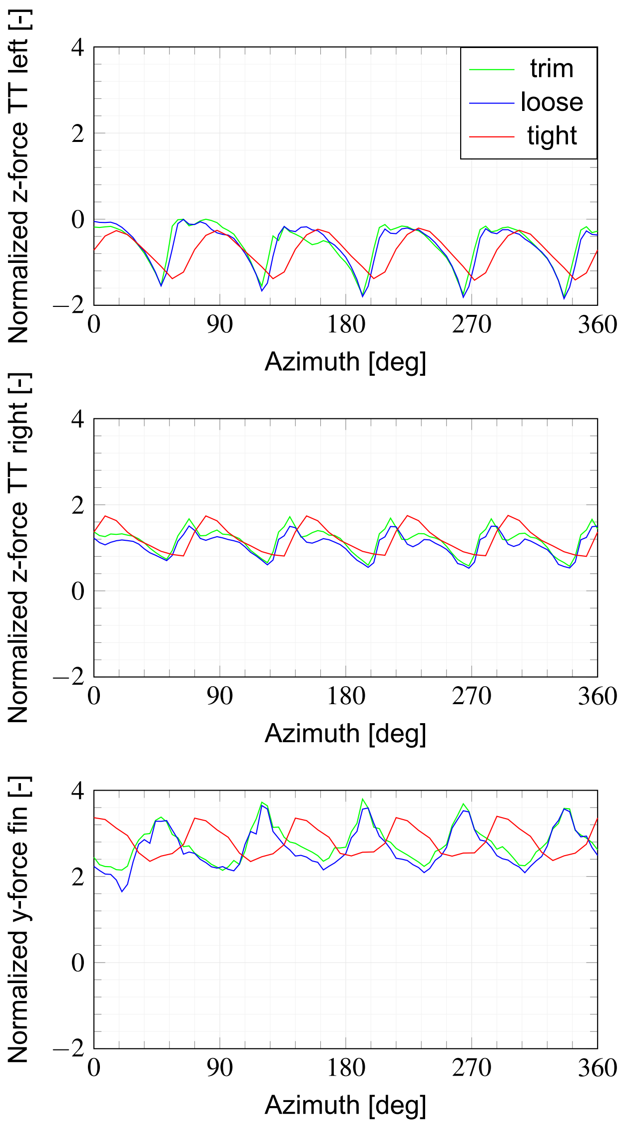

Fig. 19: Comparison of overall empennage loads between the trim coupling (trim), the loose coupling (loose), and the tight coupling (tight) for TOP36 (loads normalized by p2p y-force of the fin for loose coupling)

is comparatively too high in combination with the increased aerodynamic damping of the method.

Apart from these differences, the qualitative course of the results of the tight coupling is well comparable with the results of the loose coupling or the trim simulation. As expected, the asymmetry between the right and left side are also clearly visible in the results of the tight coupling.

3.2 PRESSURE SIGNALS

In the second step of the assessment, the pressure curves at the sensor positions on the empennage are examined. The pressure coefficient curves C_p

Table 3: Comparison of peak-to-peak empennage loads between trim coupling, loose coupling, and tight coupling for TOP36 (loads normalized by p2p y-force of the fin for loose coupling)

p2p force	Trim coupling	Loose coupling	Tight coupling
T-tail left z-force [-]	0.903	0.919	0.593
T-tail right z-force [-]	0.575	0.491	0.476
Fin y-force [-]	0.828	1.0	0.520

of the two coupling approaches are compared with the results of the flight test data. For the flight test data, the averaged curve (solid line), as well as the variations (dashed lines) are plotted on the graphs.

3.2.1 Pressure Signals T-tail

Figure 20 compares the C_p curves at the sensor positions of the T-tail (for sensor positions see Figure 3). In all graphs, as expected, a clear 5/rev fluctuation can be seen, which corresponds to the blade passing frequency (BPF) and is primarily caused by tip vortex interactions. In addition to the BPF, higher frequency components are also present in the curves, which is particularly pronounced in the signals from the upper sensors U1 and U2. In the flight test data, there is a clear difference in terms of amplitudes between the right and left side for the sensors on the lower side. The amplitudes on the right side of the T-tail are smaller than those on the left side. This suggests that the left side is closer to the tip vortices. This unequal positioning relative to the rotor wake can be attributed primarily to the asymmetry of the flow field.

Comparing the loose coupling results with the flight test data, it can be seen that the amplitudes correlate well, except for sensor positions L3 and U1. For these sensor positions, the pressure variations are significantly overestimated by UPM. The discrepancy could be caused by the significant attitude angle differences between the flight test and the simulation. Another possible explanation could be that because of the close proximity of U1 to the blade tip vortices in general, strong viscous effects occur, which are not modeled in UPM and therefore causing the amplitudes to be larger. At position L3, the different attitude angle and the simplified modeling of the fin-T-tail connection in UPM may result in a significantly different aerodynamic interaction at the fin, which in turn strongly alters the influence of the blade tip vortices. Neglecting the sensor point L3, UPM is able to reproduce the reduction of the pressure amplitude from left to right. Comparing the phases of the signals, it can be seen that they match very well for the sensors at the lower side of the T-tail. With respect to the mean, a significant offset is present for all sensor points, except for sensor L4. This offset probably stems from a combination of different influences. On the one hand, the difference in attitude angles and the resulting relative positioning to the wake has an influence, and on the other hand, it was shown in [21] that the fairings of the pressure sensors in the flight test also have a significant influence on the pressure values.

Looking at the results of the tight coupling, it can be seen that they correlate very closely with the results of the loose coupling. However, a reduction of the amplitudes at all sensor points can be seen, as well as a slight phase shift compared to the curves of the loose coupling. The smaller amplitudes are probably caused by an increased aerodynamic damping, since the aeroelastic interactions are better reproduced by the time-resolved coupling with 3D mapping. As a result, the tight coupling results correlate better with the flight test data, especially at sensor point U1, where the amplitude reduction is particularly strong. Despite the shift, the phases of the tight coupling still agree well with the flight test data. Like the loose coupling, the tight coupling shows a clear offset of the mean values compared to the flight test data and, apart from sensor point L3, the tight coupling is also able to reproduce the amplitude reduction from left to right. Overall, the results of the loose and tight coupling are very comparable with a slight improvement of the data by the time-resolved coupling with 3D mapping.

3.2.2 Pressure Signals Fin

Figure 21 compares the C_p curves at the sensor positions of the fin (for sensor positions see Figure 3). Looking at the flight test data, it is clear that there are hardly any fluctuations or 5/rev components at the lower sensors (FL1/FR1). The higher up the sensors are positioned on the fin, the more pronounced the 5/rev oscillation is. It should also be noted that the amplitudes of the pressure fluctuations are larger on the right side than on the left side of the fin. Compared to the pressure oscillations at the T-tail, the oscillations at the fin are much smaller. The reason why there are hardly any fluctuations in the lower part of the fin and why the amplitudes are generally smaller than at the T-tail is probably due to the interaction of the rotor wake with the fuselage and

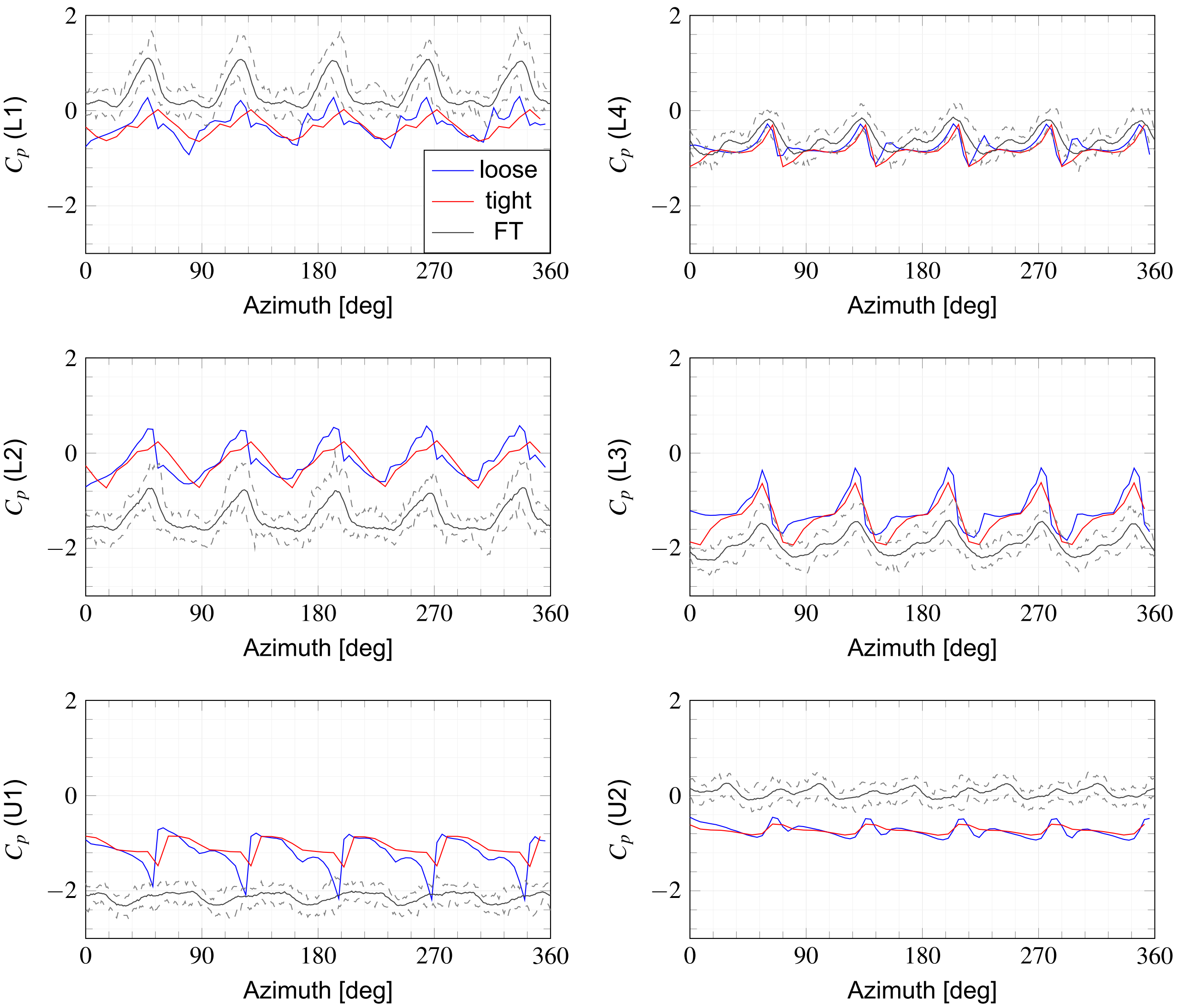

Fig. 20: Comparison of C_p values at T-tail between the flight test data (FT), the loose coupling (loose), and the tight coupling (tight) for TOP36

fairing wake. In [22] the wake structure for the TOP36 was investigated and it was shown that the wake of the fuselage and fairings directly impinges on the fin. The further down, the stronger the influence of this wake. By interacting with this wake, the rotor wake is distorted and only hits the fin in an attenuated form. As a result, the 5/rev component in the pressure curves is significantly reduced.

When analyzing the curves of the two coupling results, the 5/rev components are clearly visible. At each sensor position, the pressure variations are significantly overestimated by the coupling calculations. This is partly due to the fact that flow separations are not modeled in UPM, which also means that the wake of the fuselage is not modeled. Due to this lack of fuselage wake, the rotor wake is not affected and impinges directly on the fin, causing the strong variations with the BPF. In addition to the missing fuselage wake modeling, cutting-type interactions and viscous interactions with the boundary layer are disregarded as well, which play a significant role in direct blade vortex interactions. Such effects are usually neglected in panel methods or require special treatment. These missing viscous effects contribute as well to the fact that the amplitudes are higher in the simulation results compared to flight test measurements. Apart from this strong deviation from the flight test data, the coupling results are able to reproduce the difference between the left and right side of the fin. The amplitudes on the right side are also significantly increased compared to the left side.

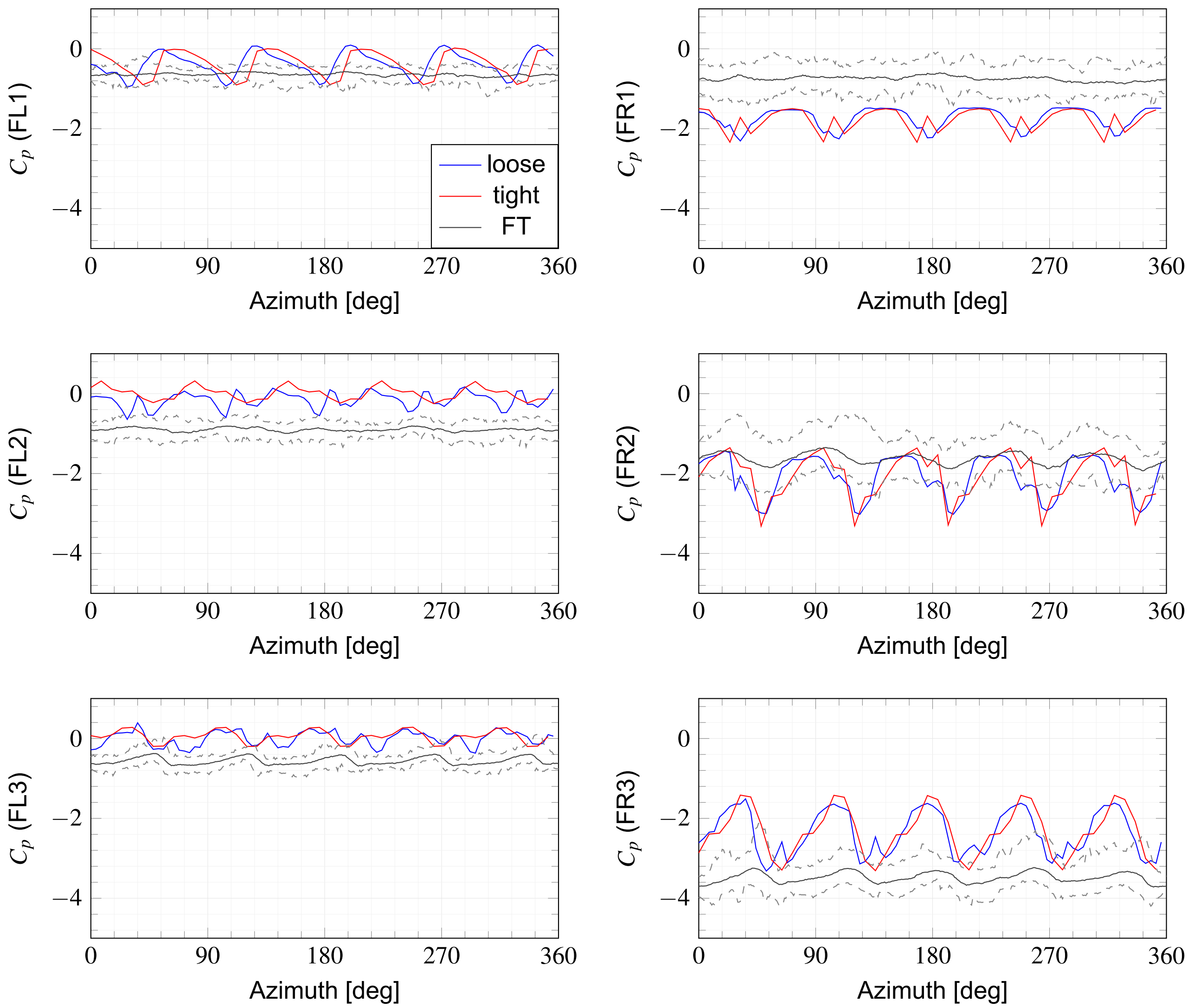

Fig. 21: Comparison of C_p values at fin between the flight test data (FT), the loose coupling (loose), and the tight coupling (tight) for TOP36

Comparing the results of the loose and tight coupling, no clear differences can be found. Only for the sensor points FL1 and FL2 a slight phase shift and reduction of the amplitude can be detected.

3.3 ACCELERATIONS

In the third step of the assessment, the vibrations of the tail boom are analyzed. For this purpose, the accelerations at the empennage sensors VFINF, VTTFLZ and VTTFRZ of the two coupling approaches are compared with the results of the flight test data. For an easy analysis, the frequency spectra are used. Since the flight test data shows strong fluctuations without a clear recurring character, the measured data is divided into sections of 3s, analyzed separately, and then averaged. For the flight test data, the averaged results (solid line), as well as the variations (dashed lines) are plotted on the graphs. For the visualization of the vibrations, the logarithmic sensor accelerations are plotted over the frequency spectrum.

Figure 22 shows the frequency spectra of the sensor VFINF at the front upper end of the fin. The longitudinal, lateral and vertical vibrations are shown. In the following, the term *low-frequency range* refers to the range between 0.5/rev and 2/rev. The structural eigenmodes lying in this range are the vertical and lateral bending modes of the tail boom, and the first two torsional modes. It is clear from the frequency spectra that there are some minor excitations of the n/rev frequencies in the vibrations calculated by the loose coupling. These peaks in the frequency spectrum are probably caused by the implementation of the loose coupling. The UPM simulation does not show perfect periodicity for the load curves. Despite an interpolation treatment this can lead to minor n/rev excitations in the structural simulation as evident in the frequency spectra. Therefore only for the BPFs the vibrations can be evaluated adequately with the loose coupling. Due to the fact that the BPF accelerations are partly about one order of magnitude larger than the average n/rev excitations, they can be evaluated quantitatively. Nevertheless, a certain variability due to the n/rev excitations must be assumed in the analysis.

Due to the time-resolved coupling, the frequency spectra of the tight coupling do not exhibit those un-physical n/rev excitations, which improves the evaluation and the significance of the results.

For the longitudinal vibrations only the first two BPFs can be evaluated quantitatively because the amplitude is significantly larger than the average n/rev excitation. For the third BPF this is not possible due to the non-negligible n/rev influence. For the first and second BPF, good agreement can be seen with a slight underestimation of the amplitude for the first and an overestimation for the second BPF compared to the flight test. Since flow separations are not modeled in UPM, the vibrations, and frequencies excited by the interactions of the airframe wake cannot be mapped. The absence of the fuselage and fairing wakes in the UPM simulation may be the reason why the vibration level of the loose coupling is at the lower limit of the variation range of the measurement data. This is because the airframe wake due to its turbulent nature usually excites a wide range of frequencies, which would raise the curve to a higher level (see also [22]).

The frequency spectrum of the tight coupling of the longitudinal vibration clearly shows that it reproduces the qualitative trend of the flight test data very well over almost the entire relevant frequency spectrum. Although the spectrum is also at the lower end of the flight test variations due to the lack of the turbulent airframe wake, there is a very high correlation between the simulation results and the measurement data. The first and second BPF are clearly seen, with the first BPF being slightly underestimated by the tight coupling and the second BPF being overestimated. A possible cause for this under- and overestimation is the fact that a constant modal damping of 4% is assumed for each mode. A specific adjustment of the damping factors might be necessary for a correct mapping. Another noticeable feature of the tight coupling frequency spectrum is the distinct peak just below 1/rev. However, this peak can in the future be eliminated by a special damping treatment and longer simulation times, similar to the approach of [22]. Apart from this un-physical peak and the missing airframe wake in UPM, the tight coupling reproduces the longitudinal vibration behavior very well.

For the lateral vibrations, the signal of the loose coupling results agrees well with the flight test data in the range between the first and second BPF. This suggests that this frequency range is particularly strongly influenced by the rotor wake. However, the first and second BPF themselves are significantly overestimated by the loose coupling. Since the amplitudes of these two frequencies are well above the average n/rev excitation, this result can be considered reasonable. The significant overestimation of the lateral vibrations of these frequencies is partly due to the fact that a modal damping of 4% was assumed for each mode. But the main reason for the significantly increased peaks is probably the not modelled airframe wake. In Figure 21 it can be seen that due to the missing airframe wake interactions in the simulation the pressure fluctuations at the fin are significantly increased compared to the measured data, which in turn leads to increased vibrations. In the frequency range below the first BPF, the curve deviates noticeably from that of the flight test data which is expected since only the main rotor wake is modeled.

Looking at the results of the tight coupling with respect to the lateral vibrations, it can be clearly seen that above the first BPF, the trend of the flight test data is very well reproduced. The simulation results are at the lower end of the flight test variations. For the first BPF again an underestimation and for the second BPF an overestimation compared to the measured data can be seen, similar to the longitudinal vibrations. Likewise, the clear peak just below 1/rev can be seen. In the frequency range below the first BPF, the tight coupling simulation results are generally significantly lower than the measured data. This could be due to the fact that the Fenestron is not modeled in the UPM model. In [22] it was shown that the lateral low-frequency oscillations are primarily caused by load fluctuations at the Fenestron. However, since the Fenestron is closed in the UPM model and UPM cannot model flow separations, the excitation of the lateral low-frequency oscillations cannot be modeled either. Another reason for the deviations is probably the missing airframe wake.

For the vertical vibrations, the course of the loose and the tight coupling results agrees well with the qualitative trend of the frequency spectrum of the

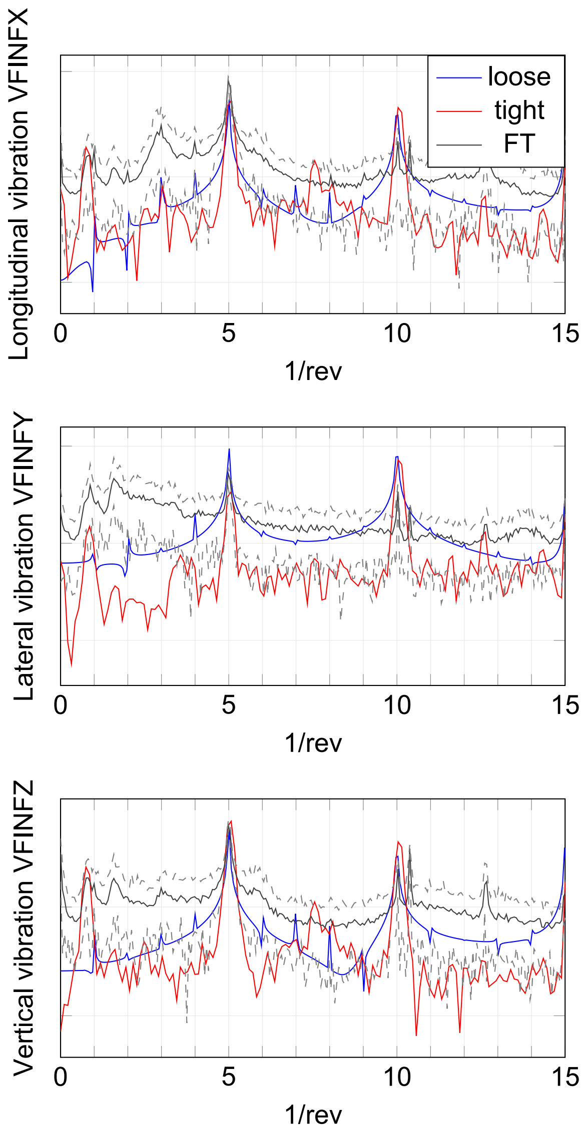

Fig. 22: Comparison of acceleration frequency spectra at fin sensor location VFINF between loose coupling simulation (loose), tight coupling simulation (tight), and flight test (FT) for TOP36

flight test data, similar to the comparison of the longitudinal vibration. For the vertical vibrations, the acceleration values of the two couplings are also at the lower end of the flight test variations. Again, the location of the vibration level at the lower boundary of the variation range is probably due to the absence of flow separation and the broadband aerodynamic turbulence in UPM. For the first BPF a good agreement can be seen compared to the flight test.

For the sensors VTTFLZ and VTTFRZ at the outer ends of the T-tail, the frequency spectra of the vertical vibrations are shown in Figure 23. For the right sensor VTTFRZ, the behavior of the loose coupling results is very similar to the behavior of the sensor VFINFZ.

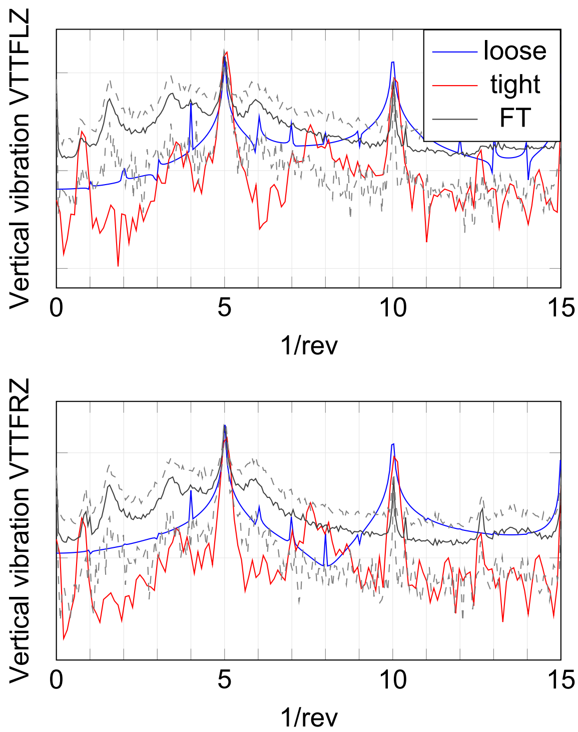

Fig. 23: Comparison of acceleration frequency spectra at T-Tail sensor locations VTTFLZ/VTTFRZ between loose coupling simulation (loose), tight coupling simulation (tight), and flight test (FT) for TOP36

However, at the left sensor VTTFLZ, the level of the frequency components above the first BPF is in the range of the flight test mean and in some cases even above it. For the first BPF for both sensors a good agreement with the flight test data can be seen in the simulation results.

For the tight coupling, the behavior is very similar for VTTFLZ and VTTFRZ. From a frequency of 3/rev upwards, the signals fit very well with the lower end of the flight test variations. The first BPF is well produced by the simulation and the second BPF is only slightly overestimated. In the low frequency range, however, the simulation again underestimates the measured data, with a stronger expression on the left side. This can possibly be explained by the absence of the airframe wake and the simplified modeling of the Fenestron, whereby primarily the first two torsional modes of the tail boom are not excited in the simulation.

4 CONCLUSIONS

Aerodynamic Loads:

1. When comparing the aerodynamic loads, there is a clear qualitative and quantitative agreement

between the load curves of the trim coupling and the loose coupling.

2. A slight offset of the curves can be identified, possibly due to the static deformation of the tail boom in the loose coupling.

3. When comparing the tight coupling results with the other two simulations a more pronounced offset can be seen, probably due to the differences in deformations.

4. The tight coupling loads have a clear phase shift compared to the other simulations, which might come from different deformation behaviour but the cause for the shift could not be clearly determined.

5. For the tight coupling an amplitude reduction can be seen, which suggests an increased aerodynamic damping.

6. All three couplings show a clear asymmetry between the right and left sides of the T-tail, which was also noted by *Rinker et al* [21] in their studies and can be explained by wake interferences at the empennage.

Pressure Signals T-Tail:

1. When comparing the pressure curves, good agreement is found for most sensor locations on the T-tail in terms of amplitude and phase.

2. The mean values show clear offsets to the flight test data, which is probably due to the different attitude angles of the helicopter compared to the flight test and due to the fairings of the pressure sensors in the flight test, since these are not modeled in the simulation (see [21]).

3. The results of the two coupling approaches correlate well, but a slight amplitude reduction and phase shift can be seen for the tight coupling results.

Pressure Signals Fin:

1. For the pressure curves at the sensor locations of the fin, significant amplitude deviations occur compared to the measured data. The coupling results clearly overestimate these.

2. The difference between the right and left side of the fin is also reproduced by the simulation results.

3. The strong deviation between simulation and flight test is probably due to the fact that in UPM the wake of the fuselage and the cutting type and viscous interactions with the boundary layer are not modeled. Such effects are usually neglected in panel methods, or require special treatment. In the flight test, there is a significant interaction between rotor and fuselage wake, which leads to a decrease in the influence of the blade tip vortices on the fin, which also reduces the amplitudes.

4. In order to reproduce the correct pressure curves at the fin, modeling and consideration of the fuselage wake is necessary in the investigated flight condition, which the current coupling methodologies cannot provide.

5. Good correlation can be found between the two coupling approaches.

Vibrations:

1. Regarding the vibrations, it can be said that when considering the vibrations at the empennage, the two coupling approaches reproduce the trend of the frequency spectra well in most areas.

2. With a few exceptions, the calculated vibration levels are at the lower limit of the variation range of the flight test data. This is probably due to the absence of the broadband turbulent content in the UPM modeling, since the turbulent wake excites a broad frequency spectrum and thus increases the vibration level.

3. Looking at the first BPF, all sensors investigated show good agreement for both coupling approaches with some slight deviations of the actual amplitude values, which is probably due to the generalized setting of the modal damping to 4%.

4. The developed loose coupling framework is well suited to represent the blade passing effects despite some methodological problems.

5. The tight coupling is able to eliminate the n/rev peaks.

6. The tight coupling shows a good correlation in large parts of the frequency range compared to the flight test results.

7. Further investigations with the tight coupling are necessary to avoid excitations of un-physical

structural response (i.e. peak below 1/rev), i.e. higher damping during the initial simulation phase and longer simulation times (similar to [22])

The results of the work show that the coupling between UPM and CSD is a promising approach for the analysis of aerodynamic interactional phenomena, but also that the current implementation is not yet sufficient for all possibly occurring phenomena. The results indicate the starting points and potential improvements that should be addressed and implemented in future studies. These necessary adjustments and optimizations are listed below:

- Essential for a correct modeling of the vibration behavior in the tight coupling is the elimination of the un-physical excitation slightly below 1/rev. For this, an additional initial coupling phase with increased damping should be implemented.
- For the analysis of many interaction phenomena, the modeling of flow separations would be additionally necessary to thereby be able to represent the fuselage wake and the resulting interferences.
- For a holistic simulation tool with a coupled flight mechanic solver for the calculation of the flight condition, an improved implementation and optimization of the FM-UPM coupling would also be necessary, in order to be able to reproduce the flight attitudes correctly. This is in fact of great importance for the aerodynamic interactions as it affects the position of the aerodynamic surfaces relative to the wake and the wake geometry itself.

Author contact:
Moritz Linder moritz.linder@tum.de
Muhammed Kürşat Yurt kursat.yurt@tum.de
Jonas John jonas.john@tum.de
Ilkay Yavrucuk ilkay.yavrucuk@tum.de

ACKNOWLEDGMENT

This work was carried out within the framework of the joint research project IDEAL-H and was funded by the Bavarian Federal Ministry for Economic Affairs, Regional Development and Energy within the scope of the Bayerische Luftfahrtforschungs- und -technologieförderung (BayLu25-II). The authors would like to express their sincere thanks to Airbus Helicopters Deutschland GmbH (AHD) for the esteemed cooperation, both in terms of professional support and in terms of providing the models and flight test data. Furthermore, we would like to thank the German Aerospace Center (DLR) for providing the freewake solver UPM and the comprehensive support.

Bavarian Ministry of Economic Affairs,
Regional Development and Energy

5 REFERENCES

[1]Wachspress, D. A., Quackenbush, T. R., and Boschitsch, A. H., “Rotorcraft interactional aerodynamics with fast vortex/fast panel methods,” *Journal of the American Helicopter Society*, Vol. 48, No. 4, 2003, pp. 223–235.

[2]Lorber, P. F., Min, B.-Y., and Wake, B. E., “Interactional aerodynamic insight obtained from wind tunnel testing and computational analysis,” 74th Annual Forum of the American Helicopter Society, Phoenix, AZ, 2018.

[3]Whitehouse, G. R., Boschitsch, A. H., and Keller, J. D., “Development and testing of a lagrangianeulerian cfd analysis for moving body and interactional aerodynamics analysis,” *AIAA Scitech 2019 Forum*, 2019, pp. 2117.

[4]Prouty, R., “The yah-64 empennage and tail rotor-a technical history,” American Helicopter Society 38th Annual Forum, St. Louis, Missouri, 1982.

[5]J. Gordon Leishman, *Principles of Helicopter Aerodynamics: Second Edition*, Cambridge University Press, Cambridge, 2nd ed., 2006.

[6]Johnson, W., *Rotorcraft aeromechanics*, Vol. 36 of *Cambridge aerospace series*, Cambridge University Press, Cambridge, 2013.

[7]Huber, H. and Polz G., “Studies on Blade-to-Blade and Rotor-Fuselage-Tail Interferences,” *Aircraft Engineering and Aerospace Technology*, Vol. 55, No. 10, 1983, pp. 2–12.

[8]de Waard, P. G. and Trouvé, M., “Tail shake vibration: Objective comparison of aerodynamic configurations in a subjective environment,” 55th American Helicopter Society Annual Forum, Montreal, Canada, May 1999.

[9]Ray W. Prouty, *Helicopter Aerodynamics: Volume I*, Eagle Eye Solutions, LLC, 2nd ed., 2009.

[10]Schäferlein, U., *Numerical Investigation of Aeroacoustic and Aeroelastic Phenomena on a Helicopter Using Higher-Order Methods*, Verlag Dr. Hut, 1st ed., 2018.

[11]ISO, "Mechanical vibration and shock - Evaluation of human exposure to whole-body vibration - Part 1: General Requirements," 01.05.1997.

[12]Mazzucchelli, C. and Wilson, F., "The Achievement of Aerodynamic Goals on the EH101 Project through the Single Site Concept," Proceedings of the 17th European Rotorcraft Forum, Berlin, Germany, September 1991.

[13]Cassier, A., Weneckers, R., and Pouradier, J.-M., "Aerodynamic Development of the Tiger Helicopter," American Helicopter Society 50th Annual Forum Proceedings, Washington, DC, May 1994.

[14]Roesch, P. and Vuillet, A., "New Designs for Improved Aerodynamic Stability on Recent Aerospatiale Helicopters," American Helicopter Society 37th Annual Forum Proceedings, New Orleans, LA, May 1981.

[15]K. C. Hansen, "Handling Qualities Design and Development of the CH-53E, UH-60A, and S-76," Royal Aeronautical Society International Conference on Helicopter Handling Qualities and Control, London, UK, November 1988.

[16]H. Huber and T. Masue, "Flight Characteristics Design and Development of the MBB/KHI BK 117 Helicopter," Seventh European Rotorcraft and Powered Lift Aircraft Forum, Garmisch-Partenkirchen, Germany, September 1981.

[17]Kampa, Konstantin, Enenkl, Bernhard, Polz, Günther, and Roth, German, "Aeromechanic Aspects in the Design of the EC135," *Journal of the American Helicopter Society*, Vol. 44, No. 2, 1999, pp. 83–93.

[18]Cao, Y. H., Wu, Z. L., and S., H. J., "Numerical Simulation of Aerodynamic Interactions among Helicopter Rotor, Fuselage, Engine and Body of Revolution," *Science China Technological Sciences*, Vol. 57, No. 6, 2014, pp. 1206–1218.

[19]O'Brien, D. and Smith, M., "Analysis of Rotor-Fuselage Interactions Using Various Rotor Models," Proceedings of the 43rd Aerospace Sciences Meeting, Reno, NV, January 2005.

[20]Renaud, T., O'Brien, D., Smith, M., and Potsdam, M., "Evaluation of Isolated Fuselage and Rotor-Fuselage Interaction Using CFD," American Helicopter Society 60th Annual Forum Proceedings, Baltimore, MD, June 2004.

[21]Rinker, M., Ries, T., Embacher, M., Platzer, S., Uhl, G., and Hajek, M., "Simulation of Rotor–Empennage Interactional Aerodynamics in Comparison to Experimental Data," Vertical Flight Society 75th Annual Forum & Technology Display, Philadelphia, Pennsylvania, May 2019.

[22]Schäferlein, U., Keßler, M., and Krämer, E., "Aeroelastic Simulation of the Tail Shake Phenomenon," *Journal of the American Helicopter Society*, Vol. 63, No. 3, 2018, pp. 1–17.

[23]Rex, W., Rinker, M., and Hajek, M., "Sensitivity Study of Helicopter Vibrations and Loads with Elastic Fuselage Coupling and Empennage Loads from Free Wake Analysis," Vertical Flight Society International 76th Annual Forum & Technology Display, Virginia Beach, Virginia, October 2020.

[24]Marius, B., Alessandro, D., Sascha, S., Sebastian, G., Florian, V., Christian, W., and Dieter, S., "Bluecopter Demonstrator - An Approach to Eco-Efficient Helicopter Design," 41st European Rotorcraft Forum, Munich, Germany, September 2015.

[25]Kunze, P., "Evaluation of an Unsteady Panel Method for the Prediction of Rotor-Rotor and Rotor-Body Interactions in Preliminary Design," 41st European Rotorcraft Forum, Munich, Germany, September 2015.

[26]J. P. Yin and S. R. Ahmed, "Helicopter Main-Rotor/Tail-Rotor Interaction," *Journal of the American Helicopter Society*, Vol. 45, No. 4, 2000, pp. 293–302.

[27]S. R. Ahmed and V. T. Vidjaja, "Unsteady Panel Method Calculation of Pressure Distribution on BO 105 Model Rotor Blades," American Helicopter Society's 50th Annual Forum, Washington, DC, May 1994.

[28]Yin, J. and Kunze, P., "DLR Free Wake Unsteady Panel Method (UPM): User Guide," .

[29]Kunze, P., "Approximate Boundary Layer Methods for a 3D Panel Code for Helicopter Simulations," 19th ONERA-DLR Aerospace Symposium, Meudon, France, June 2019.

[30]Humar, J., *Dynamics of Structures, Third Edition*, CRC Press, Hoboken, 3rd ed., 2012.

[31]Rex, W., “Corinne Report: Coupled Gensim Elastic Fuselage Framework and Validation,” Tech. rep., Technische Universität München, Februar 2019.

[32]Rex, W., “Dokumentation prefor,” Tech. rep., Technische Universität München, September 2020.

[33]Chourdakis, G., Davis, K., Rodenberg, B., Schulte, M., Simonis, F., Uekermann, B., Abrams, G., Bungartz, H., Cheung Yau, L., Desai, I., Eder, K., Hertrich, R., Lindner, F., Rusch, A., Sashko, D., Schneider, D., Totounferoush, A., Volland, D., Vollmer, P., and Koseomur, O., “preCICE v2: A sustainable and user-friendly coupling library [version 2; peer review: 2 approved],” *Open Research Europe*, Vol. 2, No. 51, 2022.